Japan Journal of Research

Original Article

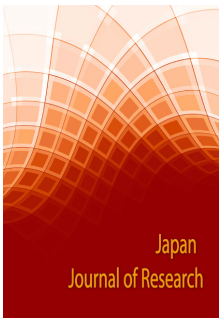

Anticorrosive–Radiative Cooling Integrated Coating for Oil Storage Tanks

Yong Wang[1], Anzhi Zhong[1], Haiyu Wang[1], Daoquan Fan[1], Yuke Li[2], Han Cheng[2], Wei Zhou[2], Xiao Xue[1,2]*

[1]Southwest Company, China National Aviation Fuel Supply Co., Ltd., Chengdu 610200, China
[2]China Southwest Architectural Design Institute Co., Ltd., Chengdu 610200, China

Correspondence
Xiao Xue
Southwest Company, China National Aviation Fuel Supply Co., Ltd., Chengdu 610200, China

- Received Date: 05 Dec 2025
- Accepted Date: 22 Dec 2025
- Publication Date: 26 Dec 2025

Keywords
oil storage tanks; radiative cooling; corrosion resistance; water-borne coating

Abstract

Oil storage tanks face critical challenges of high-temperature-induced volatile loss and corrosion failure, which restrict operational safety and economic efficiency. To address these issues, this study develops a water-based anticorrosive–radiative cooling integrated coating. The coating achieves passive cooling via solar heat reflection and radiative heat dissipation, while integrating anti-corrosion functionality to form a comprehensive protection system. Systematic optimization of key parameters was conducted: barium sulfate ($BaSO_4$) and magnesium fluoride (MgF_2) were selected as composite reflective fillers for their complementary spectral reflectivity; the optimal formulation was determined as a $BaSO_4$:MgF_2 volume ratio of 2:1, 70% pigment volume concentration (PVC), and a 150 μm coating thickness. Experimental results show that the optimized coating exhibits a solar reflectivity of up to 92.82% with stable infrared emissivity, effectively reducing tank temperature and minimizing "breathing loss" and volatile emissions. Electrochemical tests confirm that the double-layer system (epoxy–silicone anticorrosive primer and radiative cooling topcoat) maintains low-frequency impedance above 2.0×10^9 Ω after 68 days of immersion, demonstrating superior long-term corrosion resistance. As a water-borne, energy-saving, and environmentally friendly solution, the coating aligns with the "Double Carbon" goals, extends tank service life, reduces maintenance costs, and provides a sustainable protection strategy for the aviation energy storage industry, with broad application prospects in green industrial infrastructure.

Introduction

As the core infrastructure for fuel storage, metal-based oil storage tanks (predominantly fixed-roof atmospheric metal tanks, accounting for ~80% of total oil tanks) have long faced two critical challenges—high-temperature-induced evaporation loss and corrosion failure—that severely restrict their safe operation and economic efficiency [1,2]. Notably, in the chemical and fuel storage industry, outdoor storage is preferred due to its low capital investment and location flexibility compared to permanent, high-cost indoor storage [1]; however, this preference exacerbates these issues.

In summer, metal storage tanks under direct solar radiation (with solar intensity reaching ~1000 W/m² at solar noon) often reach surface temperatures of 70–80 °C, significantly elevating the temperature of internal aviation kerosene and enhancing its volatility [1]. For instance, a 5,000 m³ storage tank in Shanghai incurs substantial daily volatile losses of this high-value fuel during summer [2]. Since aviation kerosene's vapor pressure is temperature-dependent—certain types approach the 5.2 kPa limit at 30 °C and exceed it at 40 °C—the massive accumulation of volatile oil and gas not only aggravates material loss (evaporative losses account for over 50% of total operational losses in the chemical and fuel industries [3]) but also leads to "breathing loss" via breather valves due to diurnal temperature fluctuations (accounting for over half of total natural volatile losses). These processes release aromatic hydrocarbons, sulfur compounds, and vaporized fuels through vents (designed to avoid unsafe internal pressure [4]), thief hatches, or tank leaks [5]. Such emissions pose environmental pollution risks and health hazards while violating strict emission standards, and surface fouling from dust accumulation further degrades tank appearance, undermining corporate image.

Corrosion further exacerbates the predicament. Outdoor tanks, especially those in coastal areas with high humidity and salinity, suffer severe erosion from the atmosphere and rainwater. High temperatures significantly accelerate metal corrosion, shortening tank service life and increasing leakage risks that threaten operational safety. Conventional solutions are far from adequate in addressing these intertwined issues: water spray cooling

Citation: Wang Y, Zhong A, Wang H, et al. Anticorrosive–Radiative Cooling Integrated Coating for Oil Storage Tanks Japan J Res. 2026;7(1):172

systems consume massive amounts of water and electricity while intensifying corrosion [6]; single anti-corrosion coatings (e.g., white epoxy coatings from COSCO Kansai, Hempel, and Jotun) only mitigate corrosion but fail to curb high-temperature-induced losses [7]. Moreover, traditional coatings cannot meet growing environmental requirements, forcing the industry to rely on energy-intensive auxiliary cooling equipment [8].

To tackle these challenges, this study constructs a water-based composite thermal insulation coating that achieves passive cooling through solar heat reflection and radiative heat dissipation. A key advantage of this coating is its zero additional energy consumption—by reflecting most solar radiation and emitting absorbed heat as infrared radiation through the atmospheric window, it enables effective temperature reduction without reliance on external power or water resources [9,10]. Being water-based, the coating is environmentally friendly and pollution-free, fully aligning with the concept of green development [11].

Furthermore, this study integrates the water-based composite radiative cooling coating with anti-corrosion technology to establish an integrated protection system. This system simultaneously addresses the two core issues of high-temperature loss and corrosion failure in oil storage tanks [1]: it reduces volatile losses and "breathing loss" by lowering tank surface and internal temperatures, and inhibits metal corrosion by forming a durable anti-corrosion barrier [12–14]. The integrated solution not only enhances operational safety and extends tank service life but also reduces maintenance costs and avoids environmental pollution from volatile components [14,15], thereby delivering significant economic and environmental benefits.

Under the trend toward near-zero energy consumption facility construction, industrial facilities such as storage tanks are crucial for achieving "carbon peak and carbon neutrality" goals. The water-based composite thermal insulation and anti-corrosion integrated system developed in this study provides an efficient, energy-saving, and long-lasting protection strategy for oil storage tanks, with significant practical value for promoting the green and sustainable development of the aviation energy storage industry.

Materials and methods

Materials

Water-based silicone–acrylic emulsion (solid content 45%) and water-based acrylic emulsion (solid content 45%) were purchased from Yixing Kexinde Chemical Co., Ltd. Styrene–acrylic emulsion (Acronal ECO 7080) was supplied by BASF. The leveling agent (BYK-333) was obtained from BYK. Defoamer (DC65) was purchased from Dow Corning. Dispersant (SN5040) was supplied by San Nopco (Japan). The wetting agent was obtained from Yixing Kexinde Chemical Co., Ltd. Barium sulfate (AR grade) was purchased from Macklin, while barium sulfate (FIXE Micro) was supplied by Sahalee. Magnesium fluoride (AR grade), calcium fluoride (AR grade), silicon carbide (AR grade), zinc oxide (AR grade), and zinc sulfide (AR grade) were obtained from Macklin. Rutile titanium dioxide (RTC30) was supplied by DuPont.

Fabrication of the Coatings

Fabrication of the Radiative Cooling Coatings

The basic formulation of the coatings consists of 10%–16% emulsion (as adhesive), 30%–50% barium sulfate (main reflective filler), 8%–23% magnesium fluoride (main reflective filler), 0.3%–0.6% defoamer (to eliminate dispersion bubbles), 0.2%–0.4% dispersant (to improve filler dispersibility), 0.1%–0.3% wetting agent (to reduce filler surface tension), 0.2% leveling agent (to enhance coating smoothness and uniformity), 0.3%–0.5% thickener (to adjust coating viscosity), and deionized water (as diluent, to make the total mass fraction 100%).

First, an appropriate amount of deionized water was added to a 500 mL plastic beaker, followed by the addition of the wetting agent (0.1%–0.3%) and dispersant (0.2%–0.4%). The mixture was magnetically stirred for several minutes to obtain Mixture 1. Subsequently, the thermal insulation fillers (30%–50% barium sulfate and 8%–23% magnesium fluoride) and one-third of the defoamer (0.1%–0.2%) were added to Mixture 1. The resulting mixture was stirred and ultrasonicated for 20 minutes to prepare Mixture 2.

After that, Mixture 2 was thoroughly sheared and ground (using zirconium beads with a diameter of 2 mm as the grinding medium) to form a uniformly dispersed fine paste. Next, the emulsion (10%–16%) and another one-third of the defoamer (0.1%–0.2%) were added to the paste. The rotation speed was reduced, and further grinding and shearing were conducted, followed by standing to remove bubbles, thus obtaining a semi-finished product. Finally, the remaining defoamer (0.1%–0.2%) and leveling agent (0.2%) were added to improve coating performance. The viscosity of the coating was adjusted with deionized water (to make the total mass reach 100%) and thickener (0.3%–0.5%), and all components were mixed at a low speed to obtain the final coating product.

Fabrication of the Anticorrosive–Radiative Cooling Integrated Coating

Aluminum sheets were sequentially polished on a polishing machine using 800-mesh, 1200-mesh, and 2500-mesh sandpapers, followed by ultrasonic cleaning with ethanol. Prior to applying the anticorrosive primer, epoxy silicone resin and curing agent were thoroughly mixed at a mass ratio of 4:1. The mixture was then coated onto the treated aluminum sheets using a 60 μm wire-wound bar coater and cured at room temperature for 24 hours, resulting in a cured epoxy silicone anticorrosive coating thickness of 40 μm ± 2 μm.

Subsequently, a self-prepared thermal insulation and energy-saving coating was uniformly brushed onto the primer to form a 150 μm-thick thermal insulation layer, thereby completing the preparation of the double-layer coating system for the anticorrosive–radiative cooling integrated functional coating.

Characterization of the Multifunctional Coatings

The performance characterization of the prepared coatings was carried out in strict accordance with relevant national standards and academic research norms. The specific test items, instruments, and methods are described as follows:

Reflectance Spectroscopy Test

A UV–Vis–NIR spectrophotometer is capable of testing the absorption, transmission, diffuse reflection, and scattering properties of samples. In this study, a Lambda 950 UV–Vis–NIR spectrophotometer (PerkinElmer) equipped with an integrating sphere accessory was employed to measure the reflectivity of the coatings. The test range was set from 250 nm to 2500 nm, with a sampling interval of 0.5 nm.

For sample preparation, the coating was applied to a 2 × 2 × 0.5 cm aluminum sheet. Prior to coating, the aluminum surface was polished using 2000-grit sandpaper on a polishing machine and wiped clean with anhydrous ethanol. After complete

evaporation of the ethanol, the coating was asspplied by brush painting and dried at room temperature for 24 hours before testing. The solar reflectivity within a specific wavelength range was calculated using the following formula [16]:

$$R_{(\lambda_1-\lambda_2)} = \frac{\int_{\lambda_1}^{\lambda_2} R_{(\lambda)} E_{b(\lambda)} d\lambda}{\int_{\lambda_1}^{\lambda_2} E_{b(\lambda)} d\lambda}$$

$R_{(\lambda1 - \lambda2)}$ denotes the average solar reflectivity within the wavelength range of λ1 to λ2;

$R_{(\lambda)}$ is the reflectivity corresponding to a specific wavelength λ;

$E_{(\lambda)}$ represents the solar irradiance at the specific wavelength λ, in accordance with the standard ASTM G173-03 (2012).

Infrared Emissivity Test

A Fourier Transform Infrared (FTIR) spectrometer enables quantitative and qualitative analysis of samples, providing information on chemical bonds, chemical composition, and molecular structure. However, FTIR cannot directly measure the infrared emissivity of samples; instead, this parameter can be indirectly derived from reflectivity data based on Kirchhoff's law. In this work, a Nicolet iS50 FTIR spectrometer manufactured by Thermo Fisher Scientific (USA) was used, equipped with an integrating sphere accessory to measure sample reflectivity. The test range was set from 4000 cm^{-1} to 400 cm^{-1}, with a resolution of 4 cm^{-1}.

According to Kirchhoff's law, for opaque objects, emissivity equals absorptivity and can be expressed as:

emissivity = absorptivity = 1 − reflectivity.

Thus, the infrared emissivity of the coating was indirectly determined from the reflectivity data. The average infrared emissivity of the sample within a specific wavelength range was calculated using the following formula:

$$E_{(\lambda_1-\lambda_2)} = \frac{\int_{\lambda_1}^{\lambda_2} E_{(\lambda)} M_{b(\lambda)} d\lambda}{\int_{\lambda_1}^{\lambda_2} M_{b(\lambda)} d\lambda}$$

$E_{(\lambda1 - \lambda2)}$ is the average emissivity within the wavelength range of λ_1 to λ_2;

$E_{(\lambda)}$ denotes the emissivity of the sample at the specific wavelength λ; , calculated as 1- $R_{(\lambda)}$

$M_{b(\lambda)}$ represents the blackbody irradiance

Radiative Cooling Performance Test

The thermal insulation performance of the coating was evaluated using a self-designed thermal insulation test device. The device mainly consists of a constant-temperature heat source, a thermal insulation box, a temperature sensor, and a data acquisition system. First, the coating was uniformly applied to a Q235 steel plate with dimensions of 150 mm × 150 mm × 2 mm and cured at room temperature for 7 days to form a coating film with a thickness of (100 ± 5) μm. The coated steel plate was then placed in the thermal insulation box, and the distance between the coating surface and the constant-temperature heat source was fixed at 10 cm. The heat source was set to a constant temperature of 150 °C, and temperature changes on the back surface of the steel plate (non-coated surface) were recorded every 5 minutes using a temperature sensor. After the temperature stabilized, the temperature difference between the back surface of the coated steel plate and that of a blank steel plate (without coating) was calculated to characterize the thermal insulation effect of the coating. Each sample was tested three times, and the average value was taken as the final result.

Coating Surface Morphology Test:

An ultra-depth-of-field microscope integrates stereomicroscopic and metallographic microscopic technologies, enabling observation of microstructures that traditional optical microscopes cannot capture due to insufficient depth of field. A Leica DVM6 ultra-depth-of-field microscope (Leica, Germany) was used to characterize the three-dimensional surface morphology of the coatings.

Because some samples in this study were smooth white coatings, it was difficult for the ultra-depth-of-field optical microscope to distinguish surface height variations. To obtain clear three-dimensional images, the coating samples were stained prior to testing. Specifically, a PET film was marked with a neutral pen, and the colored PET film was gently scraped across the sample surface to transfer dye. During observation, a high-magnification objective lens was employed.

Corrosion Electrochemical Performance Test

For electrochemical corrosion resistance testing, the exposed surface in contact with the electrolyte was retained, while the remaining areas were sealed with epoxy resin to eliminate interference from extraneous factors. A Reference 3000 electrochemical workstation (Gamry Instruments, USA) was used for the measurements. A saturated calomel electrode (SCE) served as the reference electrode, a platinum electrode as the counter electrode, and a 3.5% NaCl solution as the electrolyte. The working electrode area was 4.9 cm^2, the frequency range was 0.01 Hz to 10,000 Hz, and the sine-wave amplitude was 10 mV. Prior to each test, the open-circuit potential (OCP) was monitored for 600 s. The coatings were immersed in the NaCl solution, and measurements were conducted at regular intervals. To minimize electromagnetic interference, all tests were performed in a shielding box at room temperature.

Results

Optical Properties of the Coating

Selection of the Functional Filler System

When the band gap width of a material matches the photon energy of ultraviolet radiation, the material absorbs ultraviolet light in that band. Therefore, to overcome the limitation of low reflectivity caused by the strong ultraviolet absorption of traditional fillers, it is necessary to select wide-band-gap materials.

In this study, the full-spectrum reflectivity of seven inorganic fillers—$BaSO_4$, CaF_2, MgF_2, RTC30 (TiO_2), SiC, ZnO, and ZnS—was measured, and the results are shown in Figure 1. As observed, $BaSO_4$ and MgF_2 exhibit significantly higher reflectivity in the ultraviolet region. In the visible light range, the reflectivity of MgF_2 approaches 100%, whereas in the near-infrared region, $BaSO_4$ shows higher overall reflectivity than MgF_2. The specific reflectivity values in different spectral bands are summarized in Table 1. These two fillers not only avoid strong ultraviolet absorption but also exhibit complementary reflectivity characteristics in the visible and near-infrared regions. Therefore, compounding these two fillers is expected to yield coatings with high overall reflectivity.

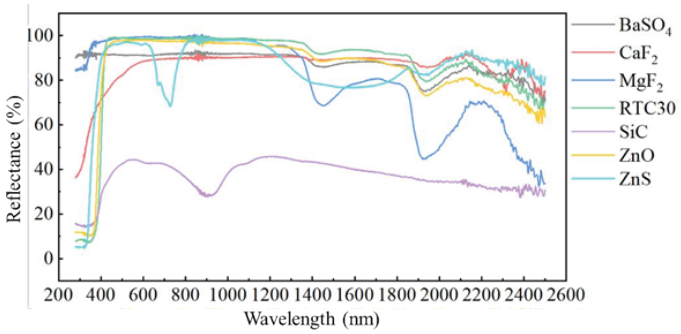

Figure 1. *Solar reflective spectrum of the prepared coatings with different fillers*

Table 1. *Reflectivity of MgF_2 and $BaSO_4$ in different spectrum region*

	Spectrum Region	MgF_2	$BaSO_4$
Spectrum Reflectivity	Solar	95.72%	93.69%
	UV	93.98%	88.07%
	Visible	99.00%	94.67%
	NIR	91.94%	93.10%

Influence of Different Filler Volume Concentrations

Pigment Volume Concentration (PVC) refers to the volume fraction of filler in the dry coating film. For coatings containing two types of fillers, the PVC is calculated using the following formula:

$$PVC = \frac{\frac{m_1}{\rho_1} + \frac{m_2}{\rho_2}}{\frac{m_1}{\rho_1} + \frac{m_2}{\rho_2} + \frac{Mw}{\rho}}$$

where ρ1 and ρ2 are the densities of the two fillers, respectively; m1 and m2 are the masses of the two fillers, respectively; M is the mass of the emulsion; w denotes the solid content of the emulsion; and ρ is the dry film density of the resin.

In the investigation of pigment properties, MgF_2 and $BaSO_4$ were selected as reflective and thermal insulation fillers. The refractive indices of MgF_2 and $BaSO_4$ are 1.390 and 1.649, respectively, which are lower than those of commonly used reflective pigments such as titanium dioxide, resulting in lower

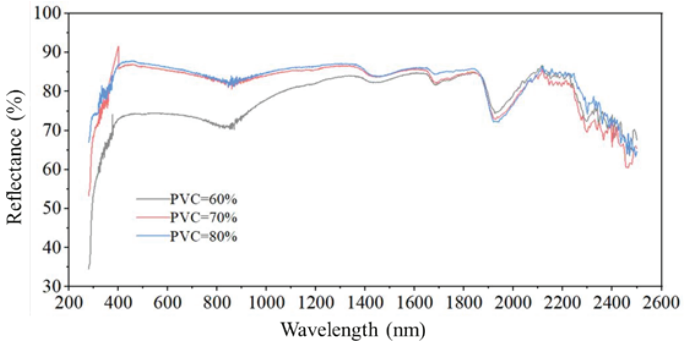

Figure 2. *Reflectivity of coatings with different PVC*

Table 2. *Reflectivity of coatings with different PVC in different spectrum region*

	Spectrum Region	60%	70%	80%
Spectrum Reflectivity	Solar	75.44%	84.54%	85.21%
	UV	67.69%	82.21%	81.77%
	Visible	73.89%	85.48%	86.21%
	NIR	78.17%	83.65%	84.35%

hiding power. To achieve strong light scattering, the filler volume concentration is therefore a crucial factor. Generally, higher PVC values correspond to higher reflectivity. In this section, a composite coating with a $BaSO_4$-to-MgF_2 volume ratio of 1:1 was used as a representative example to investigate the influence of three PVC values (60%, 70%, and 80%) on coating properties was investigated.

Figure 2 shows the reflectance spectra of coatings with different PVC values. All three coatings exhibit similar variation trends across different wavelengths. As PVC increases, the reflectivity of the coating in each spectral band increases significantly. Compared with the coating at PVC = 80%, although the PVC of the coating at PVC = 70% is lower by 10%, the average reflectivity in each spectral band and across the full spectrum differs only slightly. As shown in Table 2, the full-spectrum reflectivity of the coating with PVC = 70% is only 0.67% lower than that of the coating with PVC = 80%, and the reflectivity difference in each specific band is less than 1%.

According to Mie theory [17], based on the multiple-scattering model, the scattering capacity (or scattering intensity) of filler particles generally increases with increasing concentration only at low filler concentrations but decreases at higher concentrations. As the concentration increases, the distance between filler particles decreases, leading to interactions and obstruction among scattered light from individual particles. Under identical processing conditions, higher PVC values

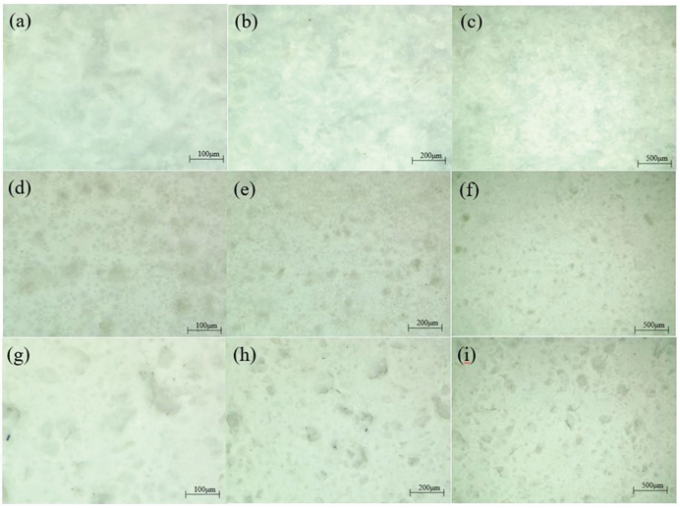

Figure 3. *Surface morphology of coatings with different PVC. (a) ~ (c) PVC = 60%, the magnification is X100, X200 and X400 respectively; (d) ~ (f) PVC =70%, the magnification is X100, X200 and X400 respectively; (g) ~ (i) PVC =80%, the magnification is X100, X200 and X400 respectively;*

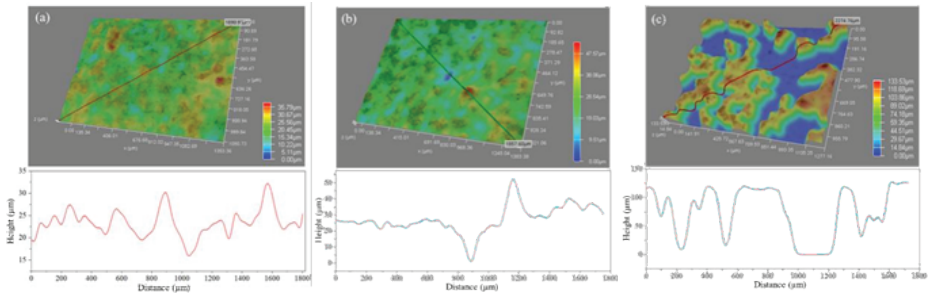

Figure 4. *3D morphology of coating surfaces with different PVC. (a)PVC=60%; (b)PVC=70%; (c)PVC=80*

promote filler agglomeration, increasing the average particle size. Longer wavelengths are preferentially scattered, while the scattering capacity for shorter wavelengths decreases. Consequently, the reflectivity of the coating with PVC = 80% decreases in the shorter-wavelength ultraviolet region.

Figure 3 shows the two-dimensional morphology of the coating surfaces with different PVC values. To make the results more representative, images of the three coatings were taken at different magnifications. Figure 4 shows the three-dimensional morphology and the corresponding surface peak–valley height curves of the coating surfaces with different PVC values. It can be easily seen from the two-dimensional planar images that, with increasing PVC, more defects such as cracks and protrusions appear on the coating surface. From the three-dimensional images, it can be more intuitively observed that the surfaces of the coatings with PVC = 60% and 70% occasionally have protrusions of about 40 μm, and the overall height fluctuation is within 10 μm, indicating a relatively flat and smooth surface. In contrast, the peak–valley difference of the coating surface with PVC = 80% reaches 133.53 μm, resulting in a more undulating and rough surface, which is not conducive to improving reflectivity. Based on the above analysis, the coating with PVC = 70% exhibits a smooth surface, reduced raw material consumption, and high reflectivity, making it the optimal pigment volume concentration.

Influence of Different Compound Ratios

In Figure 1, the optical properties of MgF_2 and $BaSO_4$ fillers were analyzed, and it was found that the two exhibit complementary advantages in reflectivity across different spectral bands. Therefore, they were compounded to obtain a coating with higher reflectivity.

The compound ratio refers to the volume ratio of the fillers. The PVC of all coatings was fixed at 70%, and the coating thickness was 50 μm. It can be observed that although the compound ratio changes, the reflectivity curves exhibit a similar overall trend.

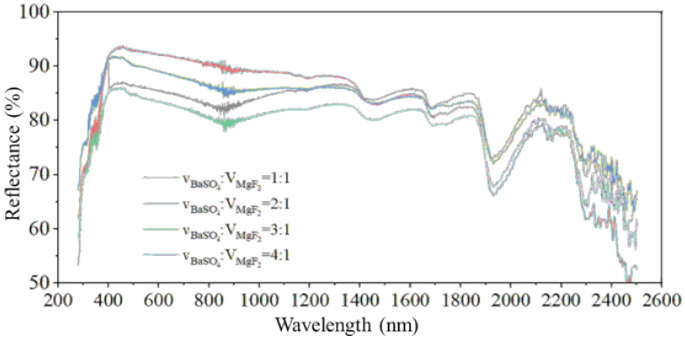

Figure 5. *Reflectivity of coatings with different compound ratios.*

The specific average reflectivity values in each wavelength range are listed in Table 3. With increasing MgF_2 content, the full-spectrum average reflectivity of the coating first increases and then decreases. When the MgF_2 content increases from 1/5 to 1/3 of the total filler volume (i.e., a $BaSO_4$:MgF_2 volume ratio of 2:1), the coating reflectivity increases significantly from 82.04% to 89.45%. However, when the MgF_2 content further increases to 1/2 of the total filler volume, the reflectivity

Table 3. *Reflectivity of coatings with different compound ratios in different wave bands*

Wavelength Band	1:1	2:1	3:1	4:1
Full-spectrum reflectivity	84.54%	89.45%	87.22%	82.04%
Ultraviolet reflectivity	82.21%	82.76%	85.84%	79.20%
Visible light reflectivity	85.48%	92.19%	89.30%	83.65%
Near-infrared reflectivity	83.65%	86.81%	84.82%	80.39%

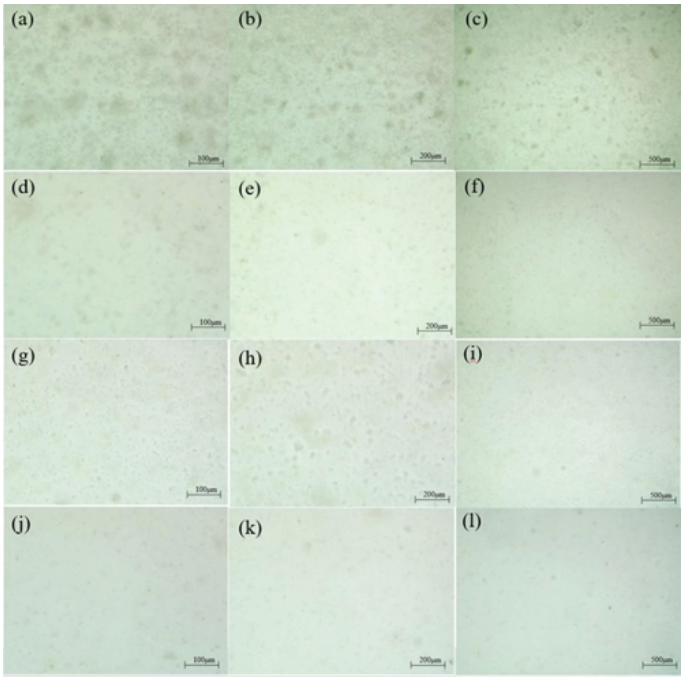

Figure 6. *Surface morphology of coatings with different composite ratios. (a) ~ (c) VBaSO4:VMgF2=1:1, the magnification is X100, X200 and X400 respectively; (d) ~ (f) VBaSO4:VMgF2=2:1, the magnification is X100, X200 and X400 respectively; (g) ~ (i) VBaSO4:VMgF2=3:1, the magnification is X100, X200 and X400 respectively;(j)~(l) VBaSO4:VMgF2=3:1, the magnification is X100, X200 and X400 respectively*

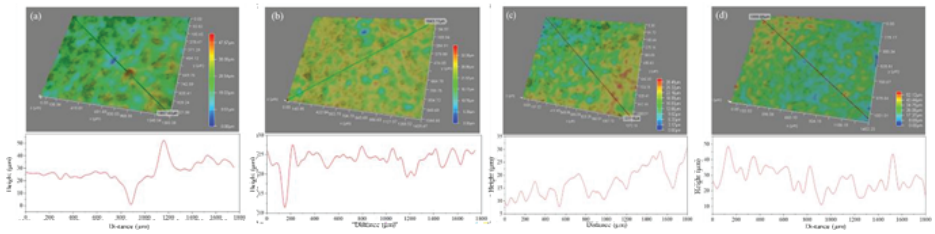

Figure 7. *Reflectivity of coatings with different compound ratios.*

decreases markedly. A comparison of the reflectivity of coatings with different ratios in the ultraviolet, visible, and near-infrared regions shows that the coating with $VBaSO_4$:$VMgF_2$=2:1 is still the highest. Therefore, from the perspective of optical performance, the optimal volume ratio of $BaSO_4$ to MgF_2 is 2:1.

Figures 6 and 7 show the two-dimensional and three-dimensional surface morphologies of coatings with different compound ratios, respectively. It can be seen from the two-dimensional planar images that the surface of the coating with $VBaSO_4$:$VMgF_2$=1:1 has significantly more defects. When the $BaSO_4$ content increases to $VBaSO_4$:$VMgF_2$=2:1, the coating surface tends to be smooth. The peak-valley height difference of the three-dimensional imaging curve represents the most prominent point on the coating surface and is not representative. From the severity of curve fluctuations and the overall color distribution of the imaging, the surface condition of the coating can be judged more comprehensively and clearly. It can be seen that the coating with $VBaSO_4$:$VMgF_2$=2:1 is more uniform, which is conducive to improving the reflectivity.

This phenomenon can be scientifically explained by the Mie scattering theory. In the coating system, when the volume ratio of $BaSO_4$ to MgF_2 is 1:1, the particle distribution is uneven, and there are more defects, which leads to significant differences in the scattering centers of the coating. At different wavelengths, the scattering efficiency varies greatly. For example, in the ultraviolet region, due to the mismatch of particle size and wavelength, the scattering intensity is low, resulting in low reflectivity. In the visible light region, although the scattering is relatively strong, the uneven distribution of particles makes the reflectivity fluctuate greatly. When the volume ratio is adjusted to 2:1, the coating surface becomes more uniform, and the particle distribution is more reasonable. At this time, for different wavelength ranges, the scattering efficiency can be optimized. In the ultraviolet band, the particle size and wavelength match better, and the scattering intensity increases, thus improving the ultraviolet reflectivity. In the visible light band, the uniform distribution of particles makes the scattering more uniform, and the reflectivity reaches a higher level. In the near-infrared band, the appropriate particle concentration and distribution make the scattering efficiency higher, which is also reflected in the higher near-infrared reflectivity in Table 3. Therefore, the more uniform coating surface of $VBaSO_4$:$VMgF_2$=2:1 makes the scattering centers more evenly distributed, which can adapt to the scattering requirements of different wavelength bands, thereby comprehensively improving the reflectivity of the coating.

To further explore the optimal compound ratio of the thermal insulation coating, outdoor temperature tests of the coating were conducted under suitable weather conditions to evaluate its thermal insulation effect, and the results are shown in Figure 8. Figure 8-a shows the test time as November 21, 2021, with

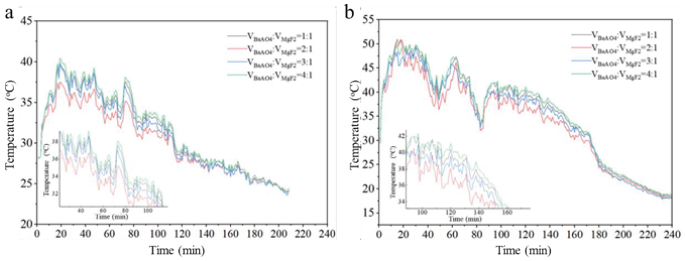

Figure 8. *Radiative cooling effect of coatings with different composite ratios: (a) test time:2024.11.21; (b) test time:2024.11.24*

a weather of sunny to cloudy, a meteorological temperature of 18 to 25°C, and a sunset time of approximately 17:40. The test started at 13:30 and ended at 17:10. Figure 8-b shows the test time as November 24, 2024, with a weather of sunny to cloudy, a meteorological temperature of 14 to 21°C, and the test started at 13:30 and ended at 17:10. It is obvious that the coating with $VBaSO_4$:$VMgF_2$=2:1 always maintains a lower temperature, which is consistent with the reflectivity results.

Influence of the Coating Thicknesses

The refractive indices of MgF_2 and $BaSO_4$ are 1.38 and 1.64, respectively, which are lower than those of traditional pigments (titanium dioxide: ; zinc oxide:). The decrease in refractive index leads to a decrease in the hiding power of the coating, which can be mitigated by increasing the coating thickness. In addition, the thicker the coating, the more coating material is required. From the perspective of cost saving, it is also necessary to explore the optimal coating thickness. In this section, coatings with thicknesses of 50 μm, 80 μm, 150 μm, and 250 μm were prepared using coatings with PVC = 70% and $VBaSO_4$:$VMgF_2$ = 2:1 for investigation.

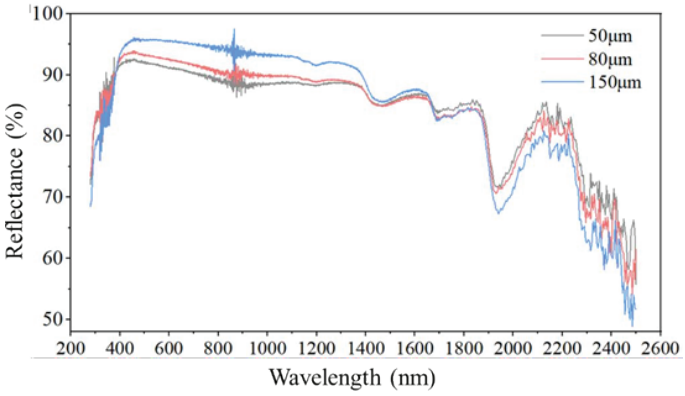

Figure 9. *Reflectivity of coatings with different thickness.*

Figure 9 shows the reflectance spectra of coatings with different thicknesses. When the coating thickness increases, the reflectivity increases significantly, especially when the thickness increases from 80 μm to 150 μm. When the coating thickness reaches 250 μm, the reflectance spectrum curve almost overlaps with that of the 150 μm thick coating. Table 4 details the specific reflectivity of coatings of each thickness in different bands. Although the near-infrared reflectivity of the 250 μm coating is higher than that of the 150 μm coating, the overall average reflectivity is 92.65%, which is almost the same as that of the 150 μm coating. From the perspective of cost saving, 150 μm is a more suitable construction thickness.

Table 4. *Reflectivity of coatings with different thickness in different spectrum region.*

	Spectrum Region	50μm	80μm	150μm
Spectrum Reflectivity	Solar	89.43%	90.36%	92.82%
	UV	88.37%	87.99%	90.44%
	Visible	91.24%	92.52%	97.32%
	NIR	87.33%	87.89%	86.54%

Figure 10 illustrates the temperature variation of coatings with thicknesses of 50 μm, 80 μm, and 150 μm over 300 minutes. In the initial stage, the temperature of all coatings rises rapidly to nearly 50 ℃, then decreases synchronously after 150 minutes, and finally approaches 20 ℃. Throughout the process, the 150 μm coating maintains the lowest temperature, demonstrating the optimal thermal insulation performance. Combined with optical properties, the 150 μm coating achieves the highest full-spectrum reflectivity (Table 4) due to its thickness matching the scattering requirements, enabling more efficient reflection of solar radiation and thus the smallest temperature rise. In contrast, the 50 μm coating has insufficient thickness, resulting in weak hiding power and low scattering efficiency, leading to a relatively higher temperature. This indicates that the coating thickness needs to match the optical design: too thin leads to insufficient thermal insulation capacity, while excessively thick (e.g., 250 μm) does not significantly improve reflectivity. In this experiment, 150 μm has achieved a balance between "reflection–thermal insulation" performance and is a more economical engineering choice.

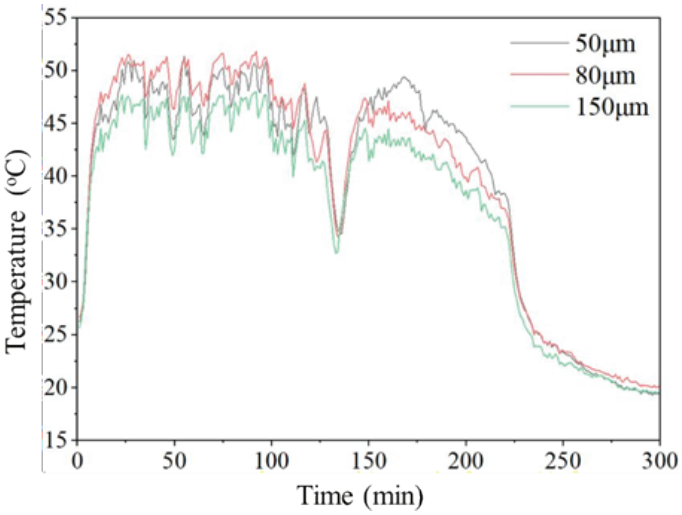

Figure 10. *Radiative cooling effect of coatings with different thickness.*

Electrochemical Performance of the Coating

Variation of $|Z|_{0.1Hz}$ with Immersion Time

Corrosion resistance is a crucial indicator for evaluating the protective performance of coatings, and the protective performance can be assessed through changes in low-frequency impedance [18,19]. Considering that low-frequency impedance is susceptible to interference in actual tests, to reduce errors, this section evaluates the variation in the protective performance of coatings by analyzing the coating impedance at a frequency of 0.1 Hz [20]. Figure 11 illustrates the changes in low-frequency impedance of the double-layer coating system and the epoxy-silicone single-layer anti-corrosion coating during long-term immersion tests.

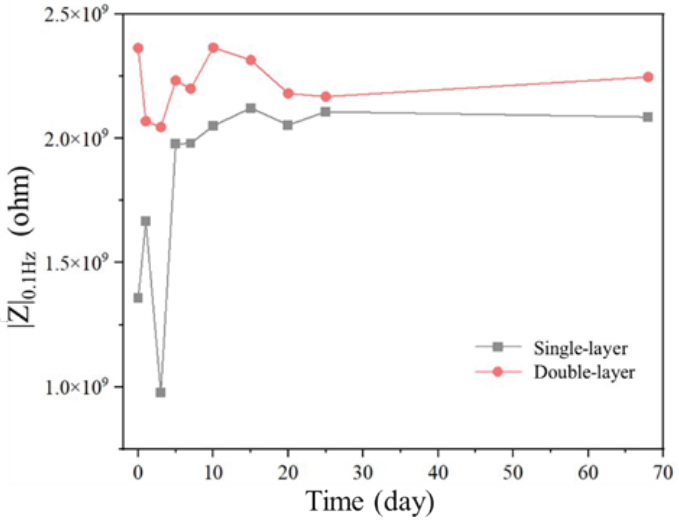

Figure 11. *Variation of $|Z|_{0.1Hz}$ with time.*

Overall, for each coating system, $|Z|_{0.1Hz}$ varied within almost the same order of magnitude and remained at a relatively high level during the 68-day immersion period, indicating that both coating systems remained intact and could provide effective barrier protection. Liu et al. [21] reported that current distributes uniformly across the entire coating area at high frequencies, while at low frequencies, it concentrates at micro-pores. Thus, the impedance of the coating at low frequencies depends on the number of micro-pores in the coating. In the initial stage of immersion, water, oxygen, and other corrosive media can rapidly diffuse through the voids and defects of the coating, leading to a certain decrease in the low-frequency impedance of each system. The $|Z|_{0.1Hz}$ of the double-layer system was 2.36×10^9 Ω, which slightly decreased to 2.05×10^9 Ω after 3 days of immersion. For the single-layer coating, the initial $|Z|_{0.1Hz}$ was 1.36×10^9 Ω, and after 48 hours of immersion, it decreased by one order of magnitude to 9.76×10^8 Ω, showing a more significant decline compared to the double-layer system.

After 3 days, the $|Z|_{0.1Hz}$ of both systems gradually increased and remained above 2.0×10^9 Ω throughout the entire immersion stage. This phenomenon may be attributed to two factors: firstly, in the initial immersion stage, substances such as water and oxygen penetrated to the metal surface through the micro-pore defects of the coating and underwent local electrochemical reactions with the metal substrate. The formed corrosion products filled the voids of the coating to a certain extent, resulting in an increase in the low-frequency impedance modulus. Secondly, when the epoxy-silicone resin, acting as the

anti-corrosion layer, came into contact with the water permeating the coating, silanol underwent a hydrolysis–condensation reaction, repairing the defects of the coating itself and thereby enhancing the barrier capacity of the coating. During the 68-day immersion period, the low-frequency impedances of the two systems were basically within the same order of magnitude, but the low-frequency impedance of the double-layer system was consistently slightly higher than that of the single-layer coating.

Changes in Electrochemical Impedance Spectroscopy (EIS)

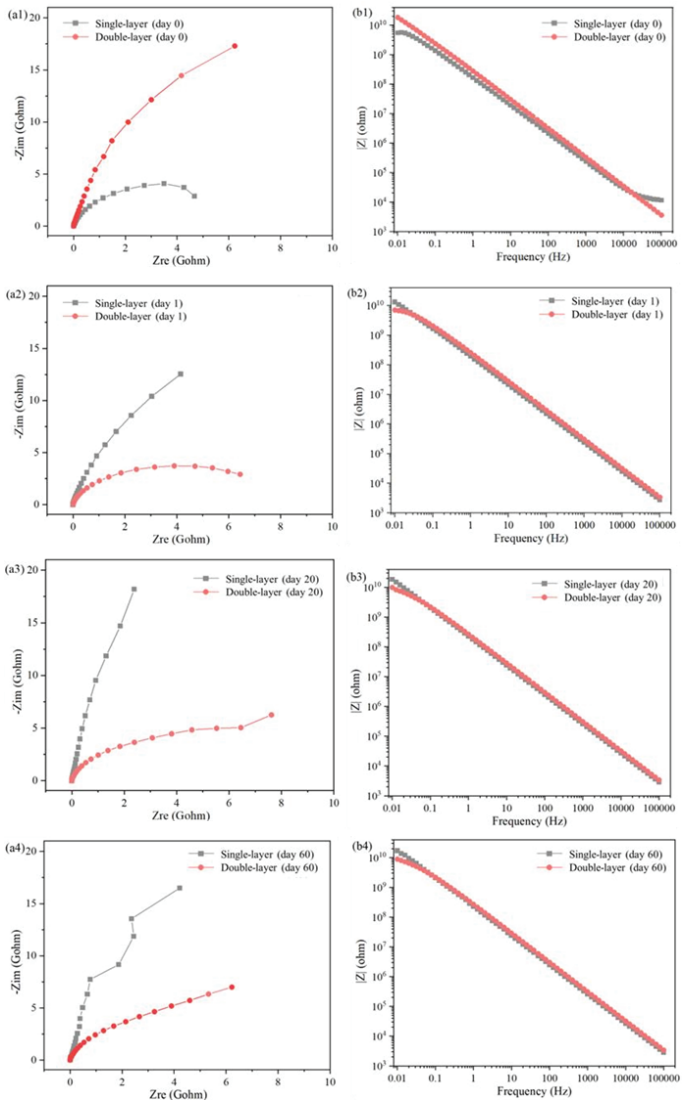

***Figure 12**. EIS of different coatings at different time periods. (a1) (b1) soak for 0.5 h; (a2) (b2) soak for 1 day; (a3) (b3) soak for 20 days; (a4) (b4) soak for 60 days.*

Figure 12 presents the electrochemical impedance spectra of the single-layer and double-layer systems after different immersion times. (a1) and (b1) are the Nyquist plot and Bode plot after immersion in 3.5% NaCl solution for 0.5 hours. In the initial stage of immersion, the Bode plots of both systems showed straight lines with an angle close to 45° with the X-axis, indicating a single time constant. The low-frequency impedance $|Z|_{0.1Hz}$ was higher than 10^9 Ω, and a circular arc with a large capacitive reactance arc was observed in the Nyquist plot. This demonstrates that both coating systems exhibited excellent barrier properties against corrosive media initially and could provide effective protection for the metal substrate. The impedance of the double-layer coating was slightly higher than that of the single-layer coating, which may be due to the superimposed barrier effect of the upper heat-insulating and energy-saving coating with a certain thickness.

Figures 12(a2) and (b2) show the electrochemical impedance spectra of the two coating systems after immersion in 3.5% NaCl solution for 1 day (24 hours). After 1 day of immersion, the low-frequency impedance of the double-layer coating slightly decreased, while that of the single-layer coating slightly increased. Correspondingly, the radius of the capacitive reactance arc of the double-layer coating decreased, and that of the single-layer coating increased. This indicates that the protective capabilities of the double-layer coating and the single-layer coating decreased and increased, respectively, after 1 day of immersion. This may be because the upper heat-insulating and energy-saving coating of the double-layer system has a porous structure, forming a sponge effect that leads to the accumulation of chloride ions and an increase in local chloride ion concentration. Nevertheless, the low-frequency impedance of the double-layer system still reached approximately 10^9 Ω, and no diffusion tail appeared in the Nyquist plot, indicating that the coating still maintained excellent protective performance.

Figures 12(a3)(b3) and (a4)(b4) show the electrochemical impedance spectra of the coatings after 20 days and 60 days of immersion, respectively. During the 60-day immersion in 3.5% NaCl solution, the electrochemical behavior of both systems did not change significantly, and the impedance spectra were similar to those after 1 day of immersion. This indicates that the epoxy-silicone coating has long-term stable protective effects, and the double-layer system constructed by combining it with the heat-insulating and energy-saving coating also exhibits excellent protective performance.

Conclusions

This study addresses the dual challenges of high-temperature-induced volatile loss and corrosion failure in oil storage tanks by developing a water-based anticorrosive-radiative cooling integrated coating. Through systematic optimization of functional fillers, pigment volume concentration (PVC), compound ratios, and coating thickness, the integrated coating achieves exceptional comprehensive performance.

The optimal formulation, featuring a $BaSO_4$:MgF_2 volume ratio of 2:1, 70% PVC, and 150 μm thickness, delivers a solar reflectivity of up to 92.82% and maintains stable infrared emissivity. This enables effective passive cooling, significantly reducing tank surface and internal temperatures, thereby minimizing "breathing loss" and volatile emissions of aviation kerosene. Electrochemical tests confirm that the double-layer system (epoxy-silicone anticorrosive primer + thermal insulation topcoat) retains high low-frequency impedance (>2.0 × 10^9 Ω) after 68 days of immersion, demonstrating long-term corrosion resistance superior to single-layer coatings.

Environmentally friendly and energy-efficient, the water-based coating avoids the high energy consumption of traditional cooling systems and the pollution risks of solvent-based products. Its application extends tank service life, lowers maintenance costs, and aligns with the "Double Carbon" goals. For the aviation energy storage industry, this integrated solution provides a sustainable protection strategy, enhancing operational

safety, economic efficiency, and environmental compliance. It also offers technical reference for radiative cooling-anticorrosion integration in other industrial storage facilities, promising broad application prospects in green infrastructure development.

Author Contributions

Y.W. and X.X. conceived the idea. Y.W., A.Z., W.Z., and X.X. designed the experiments and wrote the paper. H.W. and D.F. performed the experiments. Y.L. and H.C. analyzed the data.

Acknowledgments

The authors appreciated the financial support from the Natural Science Foundation of SiChuan (Grant No. 2024NSFSC0995) and the Key Research and Development Program of China National Aviation Fuel Supply Co., Ltd. (Grant No. HYKJ-202307).

Conflict of Interest

The authors declare no conflict of interest.

References

1. Farzaneh-Gord A. Effects of outer surface paint color on crude oil evaporative loss from the Khark Island storage tanks. Braz J Pet Gas. 2011;5(3):123-137.
2. Zhong XT. Research on reduction of evaporation loss in oil storage by high-efficiency solar heat-reflecting coating. Pet Prod Appl Res. 2004.
3. Martinez-Valencia D, Camenzind M, Wigmosta M, et al. Biomass supply chain equipment for renewable fuels production: A review. Biomass Bioenergy. 2021;148:106054.
4. Levitin R, Tryascin R. Determining fuel losses in storage tanks based on factual saturation pressures. In: IOP Conference Series: Materials Science and Engineering. IOP Publishing; 2016:012022.
5. Kalay E, Sarıoglu H, Ozkul İ. Investigation of emission control efficiency with gasoline vapor recovery units. Adv Eng Sci. 2022;2:9-14.
6. Maharjan S, Liao KS, Wang AJ, et al. Highly effective hydrophobic solar reflective coating for building materials: Increasing total solar reflectance via functionalized anatase immobilization in an organosiloxane matrix. Constr Build Mater. 2020;243.
7. Li S. Application and evaluation of new thermal insulation coatings on oil storage tanks. Petrochem Corros Prot. 2004;21(5):36-37.
8. Zhang W, Song Z, Song J, et al. A systematic laboratory study on an anticorrosive cool coating of oil storage tanks for evaporation loss control and energy conservation. Energy. 2013;58:617-627.
9. Raman AP, Anoma MA, Zhu L, et al. Passive radiative cooling below ambient air temperature under direct sunlight. Nature. 2014;515(7528):540-544.
10. Lin KT, Han J, Li K, et al. Radiative cooling: Fundamental physics, atmospheric influences, materials and structural engineering, applications and beyond. Nano Energy. 2021;80:105517.
11. Xue X, Qiu M, Li YW, et al. Creating an eco-friendly building coating with smart subambient radiative cooling. Adv Mater. 2020;32(42):1906751.
12. Lin A, Zhou MY. Functional Anti-Corrosive Coatings and Their Applications. Beijing, China: Chemical Industry Press; 2004.
13. Chen Y, Wang J, Wen S, et al. Zinc phosphate-coated modified hollow glass beads and their thermal insulation and anticorrosion performance in coatings. Ceram Int. 2021;47(16):23507-23517.
14. Zhang D, Li H, Qian H, et al. Double-layer water-borne heat insulation coatings containing hollow glass microspheres. Pigment Resin Technol. 2016;45(5):346-353.
15. Oda B, Rh B, Aeh B, et al. Fabrication of polymer-based epoxy resin as effective anti-corrosive coating for steel: Computational modeling reinforced experimental studies. Surf Interfaces. 2020;18:100454.
16. ASTM G173-03. Standard Tables for Reference Solar Spectral Irradiance at Air Mass. ASTM International; 2003.
17. Palmer BR, Stamatakis P, Bohren CF. A multiple-scattering model for opacifying particles in polymer films. J Coat Technol. 1989;61(799):41-47.
18. Martinez S, Šoić I, Špada V. Unified equivalent circuit of dielectric permittivity and porous coating formalisms for EIS probing of thick industrial-grade coatings. Prog Org Coat. 2021;153:106155.
19. Niu J, Barraza-Fierro JI, Castaneda H. Quantification of protective properties of the coating/corrosion product/steel interface by integration of transmission line model with EIS results. Coat Technol Res. 2015;12(2):393-405.
20. Bouvet G, Nguyen DD, Mallarino S, et al. Analysis of the non-ideal capacitive behavior for high-impedance organic coatings. Prog Org Coat. 2021;77(12):2045-2053.
21. Liu C, Bi Q, Leyland A, et al. An electrochemical impedance spectroscopy study of the corrosion behaviour of PVD-coated steels in 0.5 N NaCl aqueous solution: Part I. Establishment of equivalent circuits for EIS data modelling. Corros Sci. 2003;45(6):1243-1256